atmosphere

MDPI

Article

Atmospheric Drivers and Spatiotemporal Variability of Pan Evaporation Across China (2002–2018)

Shuai Li [1] and Xiang Li [2,*]

[1] Campus Security Department, Xinjiang College of Science and Technology, Korla 841000, China; lishuai78175@alumni.hust.edu.cn
[2] College of Geography and Remote Sensing Science, Xinjiang University, Urumqi 830046, China
* Correspondence: xiangli@xju.edu.cn

Abstract

Pan evaporation (PE) is widely used as an indicator of atmospheric evaporative demand and is relevant to irrigation demand and climate-related hydrological changes. Using daily records from 759 meteorological stations across China during 2002–2018, this study investigated the temporal trends, spatial patterns, and climatic controls of PE across seven major climate zones. Multiple decomposition techniques revealed a dominant annual cycle and a pronounced peak in 2018, while a decreasing interannual trend was observed nationwide. Spatial analyses showed a clear north–south contrast, with the strongest declines occurring in northern China. A random forest (RF) model was employed to quantify the contributions of climatic variables, achieving high predictive performance. RF results indicated that the dominant drivers of PE varied substantially across climate zones: sunshine duration (as a proxy for solar radiation) and air temperature mainly controlled PE in humid regions, while wind speed and relative humidity (RH) exerted stronger influences in arid and semi-arid regions. The widespread decline in northern China is consistent with concurrent changes in wind speed and sunshine duration, together with humidity conditions, which modulate evaporative demand at monthly scales. These findings highlight substantial spatial heterogeneity in PE responses to climate forcing and provide insights for drought assessment and water resource management in a warming climate.

Keywords: pan evaporation (PE); spatiotemporal variation; climate zones; meteorological factors; random forest model

Academic Editor: Gianni Bellocchi

Received: 27 November 2025
Revised: 30 December 2025
Accepted: 8 January 2026
Published: 10 January 2026

1. Introduction

Pan evaporation (PE) is a key hydrological indicator that reflects atmospheric evaporative demand and plays an essential role in estimating potential evapotranspiration (ET) and assessing regional water balance [1]. Because PE integrates the combined effects of temperature, solar radiation, wind speed, and humidity, it is widely applied in agricultural planning, drought monitoring, and water resource management [2]. Understanding the temporal variability and climatic controls of PE is therefore crucial for hydrological modeling and climate-adaptation strategies, particularly in regions facing water scarcity and frequent climate extremes [3–5].

Over recent decades, numerous studies have documented divergent PE trends across the globe, often contradicting the expected increase in evaporation associated with rising temperatures. This phenomenon—commonly referred to as the "evaporation paradox"—is especially pronounced in China, where PE trends vary substantially among regions.

Declines have been reported mainly in northern and arid areas, whereas humid and coastal regions exhibit greater temporal variability [2]. Meteorological changes such as declining wind speeds, altered solar radiation, and increasing humidity have been identified as major contributors to these patterns, in addition to land-use change and urbanization effects [1,4,6].

Given China's pronounced climatic gradients, region-specific analyses are essential for understanding PE responses to both climatic and anthropogenic drivers [7,8]. National-scale assessments have revealed a notable shift in PE behavior around the year 2000, with decreasing PE occurring despite rising actual evapotranspiration, likely linked to changes in wind speed, net radiation, and land cover [9,10]. Urbanization has also been shown to influence PE measurements, with urban stations frequently exhibiting higher PE than rural stations due to the urban heat island effect and modified surface energy balances [11].

Urban influences on PE have been further highlighted by several regional studies [12–14], which consistently demonstrate that urban stations tend to display elevated evaporation rates compared with rural counterparts [12]. For example, research in the Nanpan River Basin showed that long-term changes in PE were strongly affected by urbanization, with markedly higher PE values observed at urban sites [15]. These findings underscore the sensitivity of PE to both climatic variability and human-induced environmental change, emphasizing the need to account for regional differences when evaluating national-scale PE trends [16–18].

Despite these advances, important gaps remain. Many existing studies focus on specific regions or single climatic settings and therefore lack a unified framework for simultaneously capturing the temporal evolution and spatial heterogeneity of PE across China's diverse climate zones [19–21]. Moreover, only a limited number of studies have integrated multi-scale decomposition methods (e.g., STL, wavelet analysis, EEMD) with spatial statistical tools such as Moran's I and LISA to provide a more comprehensive characterization of PE dynamics. Another limitation is the insufficient use of recent observational data, which may restrict the accuracy of trend assessments [22–24].

To address these gaps, this study provides a climate-zone-resolved assessment of PE variability across China for the period 2002–2018. We adopt an integrated analytical framework that combines trend analysis, multi-scale decomposition, spatial pattern extraction, and machine-learning-based attribution. The specific objectives are to: (1) identify dominant temporal trends and periodic components of PE; (2) characterize the spatial heterogeneity of PE variations across seven major climate zones; and (3) quantify the climatic drivers responsible for the observed regional differences in PE. These results contribute to improved hydrological modeling and water-resource planning and provide an observational basis for interpreting PE variability along strong humidity gradients.

2. Data and Methods

2.1. Study Area and Climate Zonation

This study focuses on mainland China, a region characterized by extensive geographic diversity and a wide range of climatic conditions, spanning from humid tropical lowlands in the south to arid and cold plateau environments in the northwest. The study area covers approximately 20° N–53° N and 73° E–135° E, encompassing plains, basins, mountains, and high-elevation plateaus. Such pronounced geographic and climatic variability makes China an ideal setting for investigating spatial heterogeneity in pan evaporation (PE) and its climatic controls [25,26].

To account for regional climate differences, China was divided into seven representative climate zones based on temperature regimes, precipitation patterns, and aridity indices, following national climate classification schemes [27–29]. These zones and their standard-

ized abbreviations and shown in Figure 1, include: (1) Mid-Temperate Semi-Humid Zone (MTSH), (2) Mid-Temperate Semi-Arid Zone (MTSA), (3) Mid-Temperate Arid Zone (MTA), (4) Plateau Temperate Semi-Arid Zone (PTSA), (5) Warm Temperate Semi-Humid Zone (WTSH), (6) Northern Subtropical Humid Zone (NSTH), and (7) Marginal Tropical Humid Zone (MTHZ). These zones represent a climatic gradient ranging from arid inland regions to humid coastal and tropical environments, providing a robust framework for comparing PE trends and periodic behaviors across diverse ecological and climatic settings [30,31].

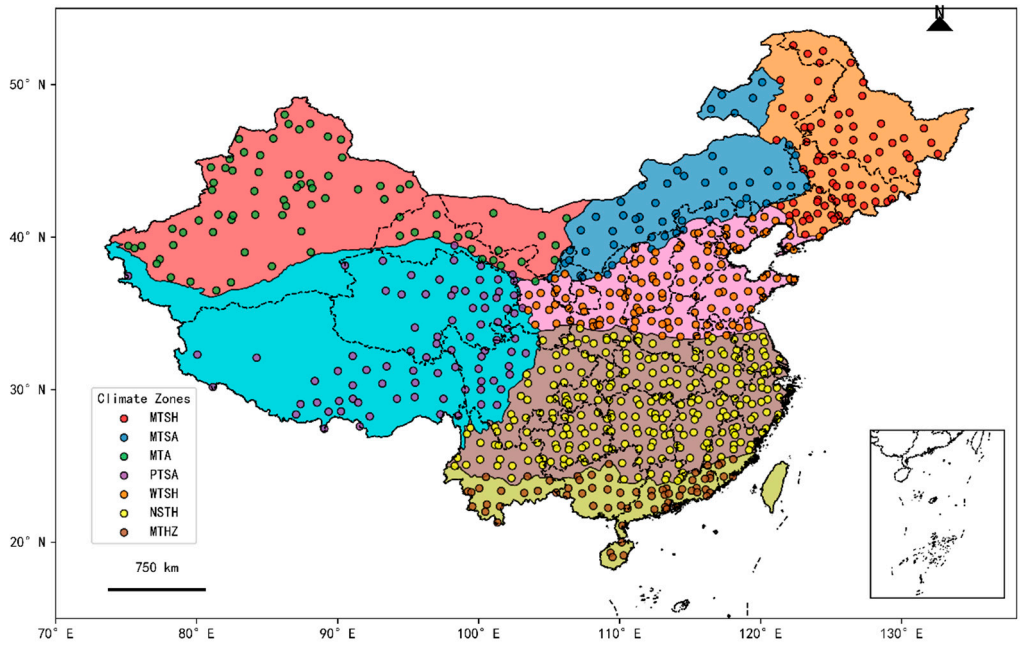

Figure 1. Spatial distribution of climate zones in China with station locations.

This zonal classification facilitates a more detailed understanding of how regional climate characteristics—such as temperature, precipitation, and atmospheric moisture—shape the spatial and temporal variability of PE. Incorporating these distinctions allows for a more comprehensive interpretation of climate–evaporation interactions at both national and regional scales.

2.2. Data Sources

The meteorological and pan evaporation (PE) data used in this study were obtained from the National Meteorological Information Center (NMIC) of the China Meteorological Administration (CMA). Specifically, we utilized the "Daily Dataset of Surface Meteorological Variables from Chinese National Ground Stations," which provides continuous daily observations from 2474 national meteorological stations across China. The dataset includes key variables such as air temperature, wind speed, relative humidity, sunshine duration, precipitation, and PE [32].

PE measurements prior to the widespread adoption of the standardized 20 cm pan evaporimeter in the 1960s may have inconsistencies [33,34]. Moreover, data completeness and station coverage improved substantially after 2000. To ensure temporal consistency, data homogeneity, and spatial comparability across stations, this study focuses on the period from 2002 to 2018, during which most stations maintained stable instrument configurations and complete daily observations. There are two types of evaporation pans used at observation stations: large-sized ones (E601B, with a diameter of 62 cm) and small-sized ones (D20, with a diameter of 20 cm). To ensure the consistency and accuracy of data, a univariate linear regression model is established for the daily evaporation amounts of large

and small evaporation pans during the overlapping observation period of each station (with the evaporation amount of the large evaporation pan as the independent variable and that of the small evaporation pan as the dependent variable) for correction. Finally, a connected daily observation sequence based on the evaporation amount of the small evaporation pan is obtained.

Following rigorous preprocessing—including CMA quality-control checks, missing-value screening, and assessments of temporal continuity—759 meteorological stations were retained for analysis. These stations met the criteria of continuous PE records, minimal missing data, and reliable metadata.

The variables used in this study include daily PE, precipitation, mean air temperature, mean wind speed, mean relative humidity, and sunshine duration. These variables support both the analysis of spatiotemporal variations in PE and the investigation of potential meteorological drivers in subsequent correlation and machine-learning analyses [35–37]. All data were spatially referenced using station latitude and longitude, and each station was assigned to one of the seven climate zones defined in Section 2.1. The station metadata for the 759 CMA sites do not provide a consistent, nationwide urban–rural classification; therefore, this study does not explicitly distinguish urban and rural stations nor include an urbanization indicator in the analysis.

2.3. Data Preprocessing

Several preprocessing procedures were applied to ensure the quality, consistency, and spatial representativeness of the PE dataset. The initial dataset contained records from 837 meteorological stations, from which 759 stations were ultimately selected based on data completeness, spatial coverage, and temporal continuity. As discussed earlier, the study period was restricted to 2002–2018 to avoid potential inconsistencies associated with instrumentation transitions or sparse observations in earlier decades. Stations with more than 5% missing annual data or pronounced temporal discontinuities were excluded.

For the retained stations, short gaps of fewer than 10 consecutive days were filled using linear interpolation, whereas longer gaps were discarded to preserve data reliability. Outliers and physically implausible values—such as negative PE observations or values exceeding climatological limits—were identified using threshold-based screening and visual inspection, and were either corrected or removed following established climate-data reconstruction practices [38–40].

To enable spatial comparison and support multivariate analyses such as EOF and EEMD, all PE time series were standardized using z-score normalization [41,42]. Each station was also assigned to one of the seven climate zones defined in Section 2.1 based on its geographic coordinates, allowing for region-specific trend analysis and periodicity assessment. These preprocessing steps ensured that the final dataset was of high quality, temporally consistent, and spatially representative across China.

2.4. Analytical Methods

To comprehensively explore the temporal and spatial variability of PE across China, we employed a structured analytical framework consisting of five categories of methods: trend analysis, periodicity analysis, spatial pattern extraction, spatial autocorrelation analysis, and zonal comparison. Each component is described below.

(1) Trend Analysis

Long-term monotonic trends in annual PE were assessed using the non-parametric Mann–Kendall (MK) test and the Sen's slope estimator [43,44]. The MK statistic S is computed as:

$$S = \sum_{i=1}^{n-1} \sum_{j=i+1}^{n} sgn(x_j - x_i), \quad with\ sgn(x) = \begin{cases} 1 & x > 0 \\ 0 & x = 0 \\ -1 & x < 0 \end{cases} \tag{1}$$

where x_i and x_j are the PE values in year i and j. If $S > 0$, it indicates an upward trend, and $S < 0$ indicates a downward trend. Sen's slope provides a robust estimate of the trend magnitude:

$$\beta = median\left(\frac{x_j - x_i}{j - i}\right), \ for\ all\ j > i \tag{2}$$

To detect potential abrupt changes, the Pettitt test was also used to identify change points within the time series [45].

(2) Periodicity Analysis

To extract seasonal and multi-year oscillatory components, we applied Seasonal-Trend decomposition using Loess (STL) decomposition, continuous wavelet transform (CWT), and ensemble empirical mode decomposition (EEMD). The STL method decomposes the original time series Y_t into:

$$Y_t = T_t + S_t + R_t \tag{3}$$

where T_t is the long-term trend, S_t is the seasonal component, and R_t is the residual or irregular fluctuation. Each component is extracted iteratively using locally weighted regression (Loess) [46].

The continuous wavelet transform (CWT) provides a time-frequency decomposition of a signal by projecting it onto a set of scaled and shifted wavelet functions [47]:

$$W_x(a,b) = \frac{1}{\sqrt{a}} \int_{-\infty}^{+\infty} x(t) \psi^* \left(\frac{t-b}{a}\right) dt \tag{4}$$

where a is the scale, b is the translation (time), and ψ^* is the complex conjugate of the wavelet function.

The EEMD decomposes the signal $x(t)$ into a set of intrinsic mode functions (IMFs) by adding finite-amplitude white noise and performing empirical mode decomposition (EMD) repeatedly [48]:

$$x(t) = \sum_{i=1}^{n} IMF_i(t) + r_n(t) \tag{5}$$

where $IMF_i(t)$ is the i-th intrinsic mode function, and $r_n(t)$ is the final residual trend component. EEMD overcomes mode mixing by ensemble averaging the decomposed results from multiple noise-added realizations [48,49].

(3) Spatial Pattern Extraction

To extract dominant spatial modes of variability and reveal regional co-variability structures, we used Empirical Orthogonal Function (EOF) analysis [50,51]. The anomaly matrix X (stations × years) was decomposed using singular value decomposition:

$$\boldsymbol{X} = \boldsymbol{U}\Sigma\boldsymbol{V}^T \tag{6}$$

where $\boldsymbol{U}$ represents spatial patterns (EOFs), $\boldsymbol{V}$ temporal patterns (PCs), and Σ is a diagonal matrix of singular values [50]. The PCs were later compared with dominant periods from CWT and EEMD to examine joint temporal evolution.

(4) Spatial Autocorrelation Analysis

To evaluate spatial dependence and clustering in PE trends and periodic signals, we calculated Global Moran's I, Local indicators of Spatial Association (LISA). Moran's I is defined as:

$$I = \frac{n}{W} \times \frac{\Sigma\Sigma w_{ij}(x_i - \bar{x})(x_j - \bar{x})}{\Sigma(x_i - \bar{x})^2} \quad (7)$$

where w_{ij} is the spatial weight and $\bar{x}$ is the global mean. We constructed a K-nearest neighbors (KNN) spatial weight matrix (k = 5) to define local spatial structure [52].

(5) Random Forest model and validation

A Random Forest (RF) regression model was employed to quantify the nonlinear contributions of meteorological variables to monthly pan evaporation (PE). Accordingly, all attribution analyses are conducted at the monthly scale to ensure consistency with the interannual–decadal focus of the study and to enable direct comparison with the annual/trend and spatial-mode diagnostics. Monthly PE was used as the target variable, and predictors were restricted to the five meteorological variables available in this study: precipitation (P), mean air temperature (Tair), mean wind speed (WS), mean relative humidity (RH), and sunshine duration (SSD).

This study focuses on spatial heterogeneity and climate-zone contrasts of PE variability across China at interannual–decadal time scales. We therefore constructed monthly PE and monthly meteorological predictors (Tair, WS, RH, P, and SSD as a radiation proxy) to reduce high-frequency synoptic noise and to improve temporal completeness across the national station network. This temporal aggregation is consistent with the time scales of our trend detection (MK/Sen), spatial mode decomposition (EOF), and spatial autocorrelation analyses (Moran's I), and facilitates physically interpretable comparisons along the humidity gradient. Monthly predictors were derived from daily observations by taking monthly means for Tair, WS and RH, monthly sums for P and SSD, and monthly mean for PE. We note, however, that monthly aggregation may damp short-duration extremes and under-represent nonlinear daily responses of PE to heatwaves or strong wind events. To address this limitation, we conducted a sensitivity experiment incorporating within-month extremes metrics derived from daily observations (Section 3.8).

To assess generalization performance and avoid information leakage across months from the same station, we adopted a station-wise independent split stratified by climate zone (70%/30% of stations within each zone; random_state = 42), ensuring that all months from a station were assigned exclusively to either training or test. The RF model was trained using a fixed hyperparameter configuration with 500 trees (n_estimators = 500) and bootstrap sampling (bootstrap = True), while other parameters were kept at their scikit-learn default values (random_state = 42; n_jobs = −1). Model performance (R^2 and MSE) was evaluated on the independent test set. Variable-importance rankings were quantified using permutation importance computed on the independent test set with repeated shuffling (n_repeats = 30), and zonal rankings were obtained by training RF models separately for each climate zone using the same predictors and evaluation protocol. The RF hyperparameter configuration used in this study is summarized in the Supplementary Materials (Table S1).

3. Results

3.1. Temporal Trends of PE

Pan evaporation (PE) from 2002 to 2018 shows clear regional contrasts across China. As illustrated in Figure 2a, most stations in northern, northeastern, and central China exhibit negative Sen's slopes, indicating a long-term monotonic decline in PE, whereas

several stations in southern and coastal regions show weakly positive but mostly non-significant changes. This spatial pattern reflects strong regional differences in meteorological conditions. At the national scale, annual mean PE shows a significant monotonic decreasing trend, with a Sen's slope of -0.015 mm day^{-1} yr^{-1} and an MK p-value of 0.0074 (Figure 2b). The decline persists from 2002 to 2017, followed by an increase in 2018. To interpret this event, we quantified 2018 anomalies of PE and key meteorological variables relative to the 2002–2017 baseline using station observations. Nationally, PE exhibits a positive anomaly of +0.877, accompanied by markedly warmer conditions (Tair: +3.388) and substantially reduced precipitation (P: −59.404), indicating a warmer and drier background that favors enhanced evaporative demand. Wind speed shows a modest positive anomaly (WS: +0.120), whereas relative humidity changes are negligible at the national scale (RH: +0.004). Sunshine duration anomalies display strong spatial heterogeneity across climate zones (Figure S2; Table S4), suggesting region-dependent radiative forcing during 2018. Overall, the 2018 PE surge is most coherently explained by the combined effects of anomalous warming and widespread precipitation deficits, with additional regional modulation by wind and radiation anomalies, consistent with the RF-identified dominant drivers.

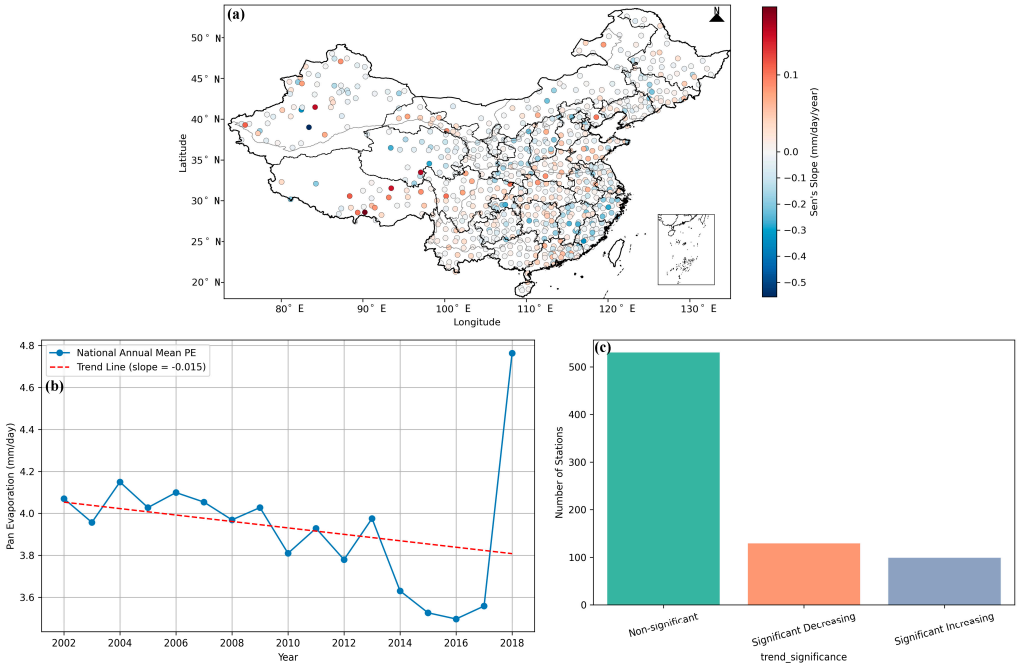

Figure 2. Temporal trends of Pan Evaporation (PE) across China (**a**) Spatial distribution of Sen's slope for station-level PE trends; (**b**) Annual mean PE in China (2002–2018) with a fitted trend line (dashed red); (**c**) Classification of station-level PE trends based on significance and direction.

Trend classifications (Figure 2c) show that approximately 70% of stations display non-significant trends, while 17% exhibit significant decreases and 13% show significant increases. Note that MK and Sen's slope provide a non-parametric assessment of monotonic change and do not imply a linear process or a constant rate of change.

Overall, the results indicate a nationwide decline in PE accompanied by substantial spatial variability, highlighting the influence of regional climatic conditions on evaporative demand.

The national annual series shows a pronounced increase in PE in 2018 (Figure 2b). To interpret this event, we quantified 2018 anomalies of key meteorological variables relative to the 2002–2017 baseline using the same station observations. Nationally, PE exhibits a positive anomaly of +0.877, accompanied by markedly warmer conditions (Tair

anomaly: +3.388) and substantially reduced precipitation (P anomaly: −59.404), consistent with enhanced atmospheric evaporative demand. Wind speed shows a modest positive anomaly (WS: +0.120), whereas relative humidity changes are small at the national scale (RH: +0.004). Sunshine duration anomalies display strong spatial heterogeneity across climate zones, indicating region-dependent radiative forcing during 2018 (Figure S2; Table S4). Overall, the 2018 PE surge is most coherently explained by the combined effects of anomalous warming and widespread precipitation deficits, with additional regional modulation by wind and radiation anomalies, consistent with the RF-identified dominant drivers.

3.2. STL Decomposition of National Monthly PE

Seasonal–Trend decomposition using Loess (STL) was applied to the national monthly PE series from 2002 to 2018 to identify dominant temporal components. As shown in Figure 3, the decomposition clearly separates the long-term trend, seasonal cycle, and residual variability.

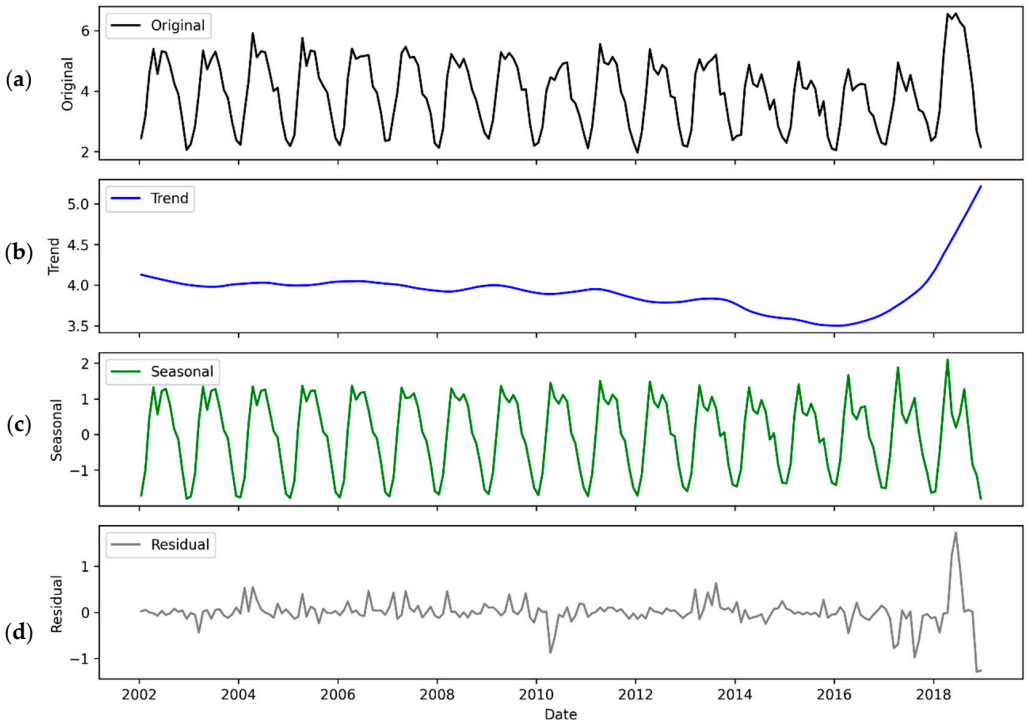

Figure 3. STL decomposition of the national monthly PE series (2002–2018), showing: (**a**) original time series, (**b**) long-term trend, (**c**) seasonal cycle, and (**d**) residual component.

The trend component shows a gradual decline in national PE from 2002 to 2016, consistent with the results in Section 3.1, followed by a marked increase in 2018. This abrupt shift reflects an exceptional anomaly in that year. The seasonal component exhibits a stable and recurring annual pattern, with higher PE in summer and lower PE in winter, driven primarily by temperature and radiation seasonality. Seasonal variability accounts for 83.7% of the total variance, indicating that seasonality is the dominant contributor to national PE fluctuations throughout the study period. The residual component captures short-term and irregular variations, with relatively small amplitudes except for a pronounced spike in 2018. The minimal residual variability suggests that interannual fluctuations play a secondary role compared with the strong seasonal and long-term components.

In summary, the STL decomposition highlights the overwhelming influence of seasonality on national PE variability, while also revealing the distinct 2018 anomaly that warrants further investigation in subsequent analyses.

3.3. Continuous Wavelet Analysis of Monthly PE

Continuous Wavelet Transform (CWT) was applied to the national monthly PE series (2002–2018) using the Morlet wavelet to identify dominant periodicities and their temporal evolution. The wavelet power spectrum (Figure 4) highlights a persistent 12-month cycle, which remains the strongest and most stable feature throughout the study period. This dominant annual periodicity is consistent with the STL results and reflects the strong seasonal control on PE across China.

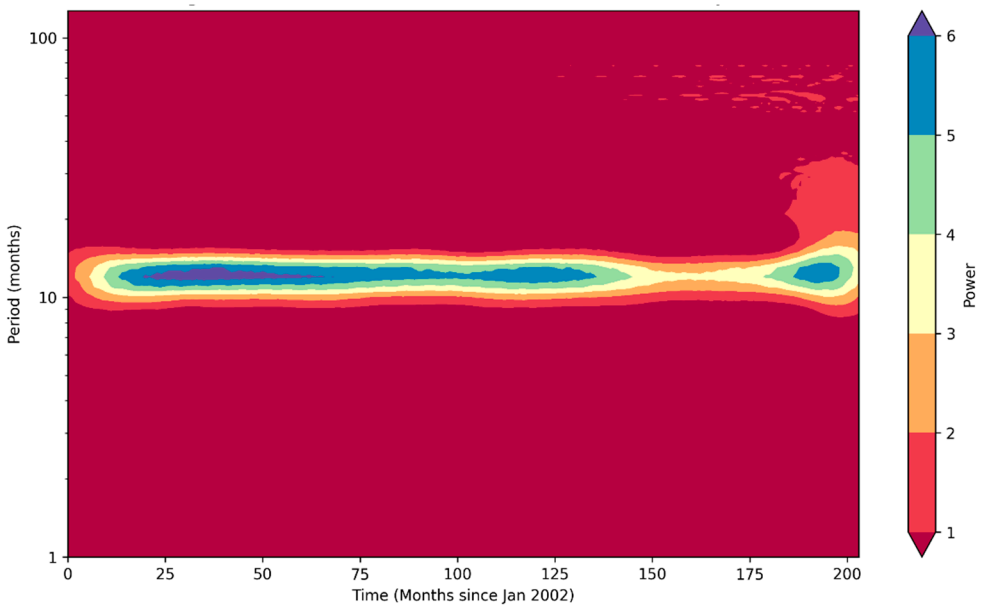

Figure 4. Continuous wavelet power spectrum of the national monthly PE series (2002–2018). The dominant energy is concentrated around the 12-month period, reflecting strong seasonal oscillation.

In addition to the annual cycle, weaker but discernible power appears in the 2–4-year band, particularly toward the end of the study period. These low-frequency oscillations indicate modest interannual variability and may reflect the influence of short-term climate oscillations. Although not dominant, their presence suggests that interannual climate fluctuations contribute to secondary variations in PE.

The amplitude of the annual cycle shows a slight strengthening after 2016, indicating enhanced seasonal contrast in recent years. However, no significant long-term shifts are observed in the timing or structure of the primary periodicities.

This provides a clear temporal structure that supports the subsequent multi-scale decomposition analysis. These findings reinforce the results of the STL decomposition and highlight the importance of both seasonal forcing and occasional low-frequency climate variability in shaping national PE dynamics.

3.4. EEMD of Monthly PE

Ensemble Empirical Mode Decomposition (EEMD) was used to extract intrinsic temporal components from the national monthly PE series for 2002–2018. The decomposition produced six intrinsic mode functions (IMFs), each representing variability at different timescales (Figure 5).

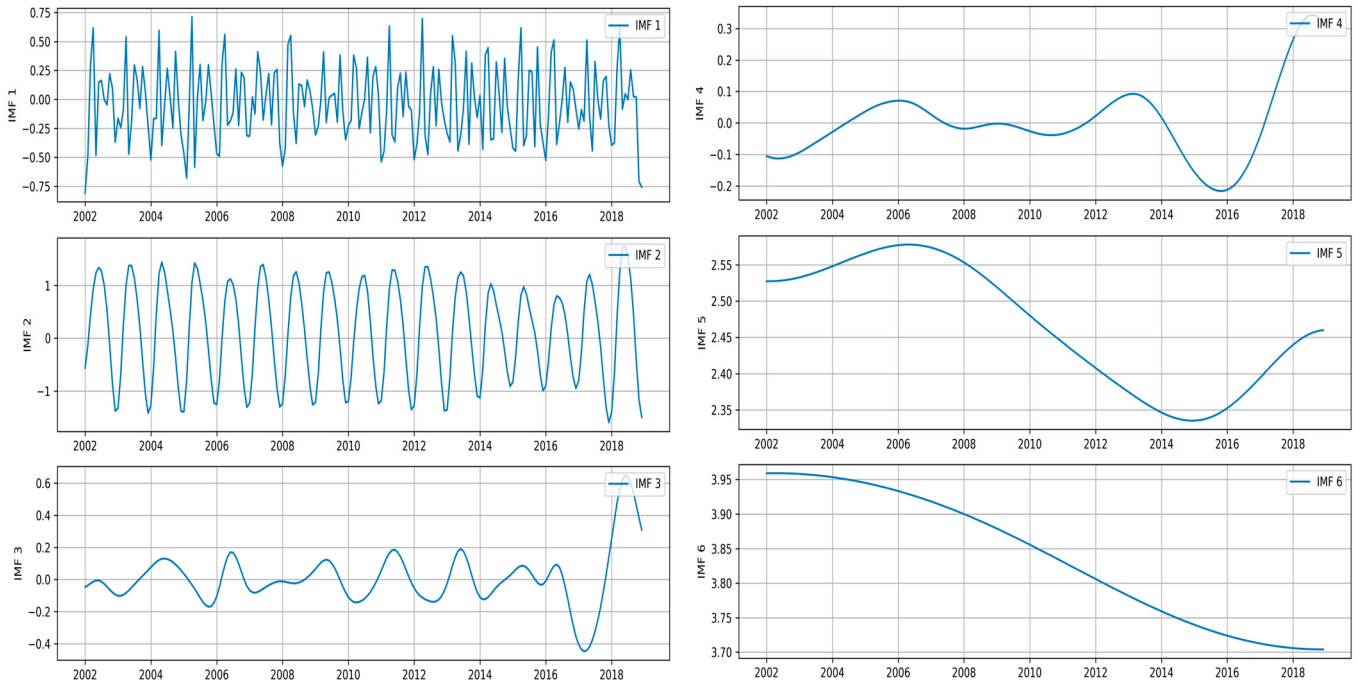

Figure 5. EEMD of the national monthly PE (2002–2018). Six intrinsic mode functions (IMFs) were extracted, ranging from high-frequency to trend components.

IMF 1 captures high-frequency fluctuations associated with short-term atmospheric variations and contributes mainly to rapid but low-amplitude changes in PE. IMF 2 exhibits a stable ~12-month periodicity that reflects the dominant annual cycle, consistent with the STL and CWT results. This IMF represents the strongest and most persistent mode of variability in the PE record. IMFs 3–5 correspond to lower-frequency oscillations, indicating modest interannual to quasi-decadal variability. These components likely reflect the influence of broad-scale climate fluctuations, although their amplitude is substantially weaker than the seasonal mode. IMF 6 represents the long-term trend and shows a gradual decline in PE from 2002 to 2016, followed by a distinct increase after 2017—mirroring the national trend identified in Section 3.1.

The EEMD results show that the annual cycle dominates national PE variability, while weaker low-frequency components reflect secondary interannual influences. This multi-scale structure provides important context for interpreting regional PE responses and for linking temporal modes with climatic drivers.

3.5. EOF Analysis

3.5.1. Variance Contribution of Leading EOF Modes

Empirical Orthogonal Function (EOF) analysis was applied to the standardized annual PE anomaly matrix to identify dominant spatiotemporal modes (Figure 6). The first EOF mode explains 46.0% of the total variance, followed by 20.1% for EOF 2. The contributions of EOF 3–6 decrease to 8.9%, 4.2%, 3.8%, and 3.1%, respectively. Together, the first six modes account for 86.2% of the total variance, indicating that most of the meaningful variability is captured by the leading modes.

Figure 6 shows that EOF1 explains 46.0% of the total variance of monthly PE anomalies, indicating a spatially coherent dominant mode. Rather than a spatially uniform 'background' signal, EOF1 represents the dominant large-scale east–west (northeastern/eastern China versus western China–Tibetan Plateau) contrast in PE anomalies, indicating opposite-phase variability between the monsoon-influenced eastern sector and the westerly/topography-controlled western interior. Importantly, these pathways directly

correspond to the dominant RF drivers identified in this study (Tair/RH/SSD and WS), providing a physically interpretable linkage between the statistical mode and meteorological controls.

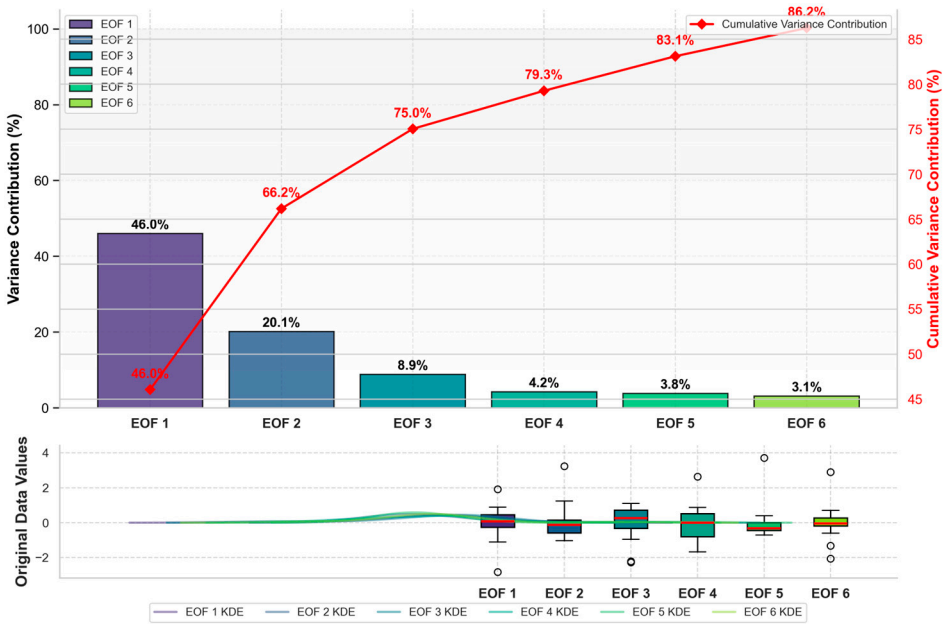

Figure 6. Variance contribution (%) and cumulative variance contribution (%) of the leading EOF modes of monthly PE anomalies. Higher variance contribution indicates a more dominant spatiotemporal mode, while the cumulative curve shows the fraction of total variance explained by the first N modes.

EOF2 (20.1%) captures a secondary regional contrast superimposed on EOF1, indicating additional out-of-phase variability among eastern sub-regions and the western interior/Plateau; this suggests that multiple circulation-linked processes contribute to PE anomalies beyond the leading east–west polarity. Such a dipole is consistent with circulation-mediated redistribution of moisture and cloudiness: variability in East Asian monsoon moisture transport and associated cloud cover can modulate RH and sunshine duration (SSD) over northeastern/eastern China, while concurrent shifts in the mid-latitude westerlies and the East Asian jet—together with Tibetan Plateau thermal–dynamic effects—can influence near-surface wind speed (WS) and radiative conditions over western China and the Plateau. This provides a mechanistic interpretation of the observed EOF2 structure beyond a purely descriptive account.

The cumulative variance curve rises sharply with the inclusion of the first two modes, confirming their dominant explanatory power. The boxplot and KDE distributions show that the leading modes have more concentrated value ranges, while higher-order modes display broader and more irregular distributions, consistent with their weaker contributions. These results indicate that the first few EOF modes effectively summarize the main spatiotemporal structure of PE variability, with higher-order modes representing minor or noise-like fluctuations.

3.5.2. Spatial Distribution of EOF

The spatial loading pattern of the first EOF mode (EOF1) captures the dominant structure of PE anomalies across China (Figure 7). EOF1 shows a coherent dipole pattern, with positive loadings over most northern and eastern regions and negative loadings across western China, including the Tibetan Plateau. This contrast reflects the primary large-scale spatial variability embedded in the national PE field.

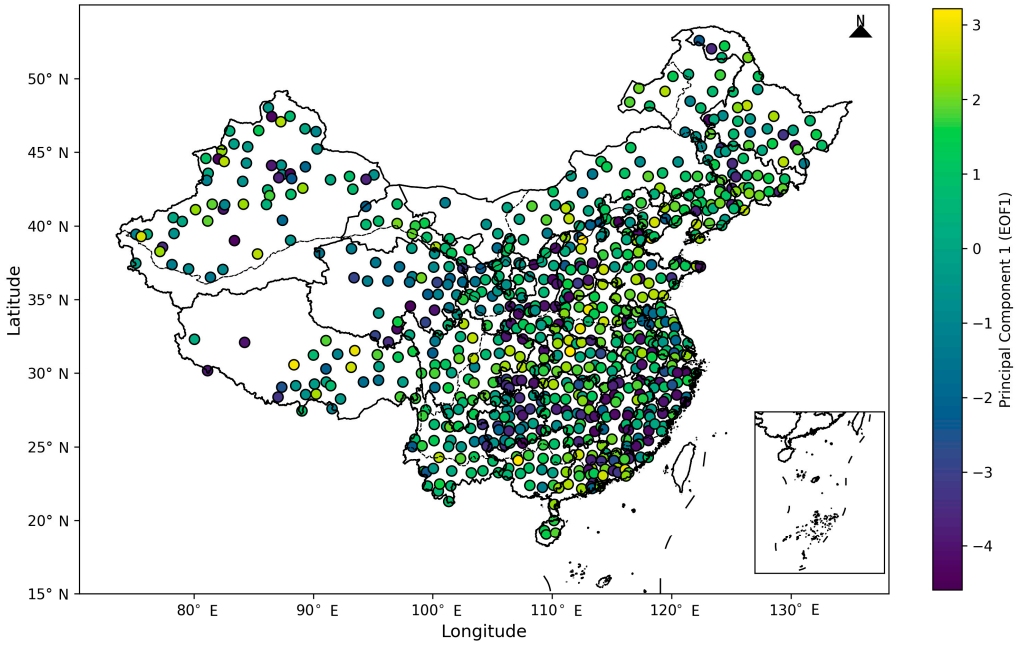

Figure 7. Spatial loading pattern of EOF1 for monthly PE anomalies. Positive (negative) loadings indicate regions where PE anomalies tend to vary in phase (out of phase) with the EOF1 time coefficient (PC1). Larger absolute loadings denote a stronger contribution of EOF1 to local PE variability.

Regions with positive loadings correspond to areas where PE anomalies tend to fluctuate coherently in the same direction, whereas negative loadings indicate opposite-phase variability. The clear spatial organization of EOF1, which explains 46.0% of the total variance, confirms its role as the leading mode characterizing nationwide PE variation. In comparison, higher-order modes capture progressively smaller and more localized variability. This dominant spatial pattern provides the primary basis for interpreting regional differences in PE anomalies and their associated large-scale variability.

This east–west (and northeast–Tibetan Plateau) polarity is consistent with the contrast between the monsoon-influenced eastern China and the westerly/topography-controlled western interior. The opposite-phase PE anomalies implied by EOF1 suggest that years with stronger continental advection and clearer-sky conditions over northern–eastern China tend to coincide with relatively suppressed evaporative demand over the Tibetan Plateau/western regions, where cloudiness and complex terrain can modulate radiation and near-surface winds. This interpretation is also consistent with the dominant importance of aerodynamic (wind speed) and energy-related (air temperature and sunshine duration) controls identified by the RF attribution, indicating that large-scale circulation–radiation–wind co-variability is embedded in the leading EOF structure.

3.5.3. EOF Time Coefficient Spatial Distribution

The spatial distribution of the time coefficients (PC1) associated with EOF1 is shown in Figure 8. Positive coefficients are predominantly observed across the southern, eastern, and parts of central China, whereas negative coefficients occur mainly in northern and western regions. This spatial contrast indicates that the leading EOF mode exhibits regionally differentiated contributions to annual PE anomalies. Stations with positive PC1 values correspond to locations where the EOF1 spatial pattern is expressed more strongly, while negative values represent locations where the same mode is expressed with opposite phase.

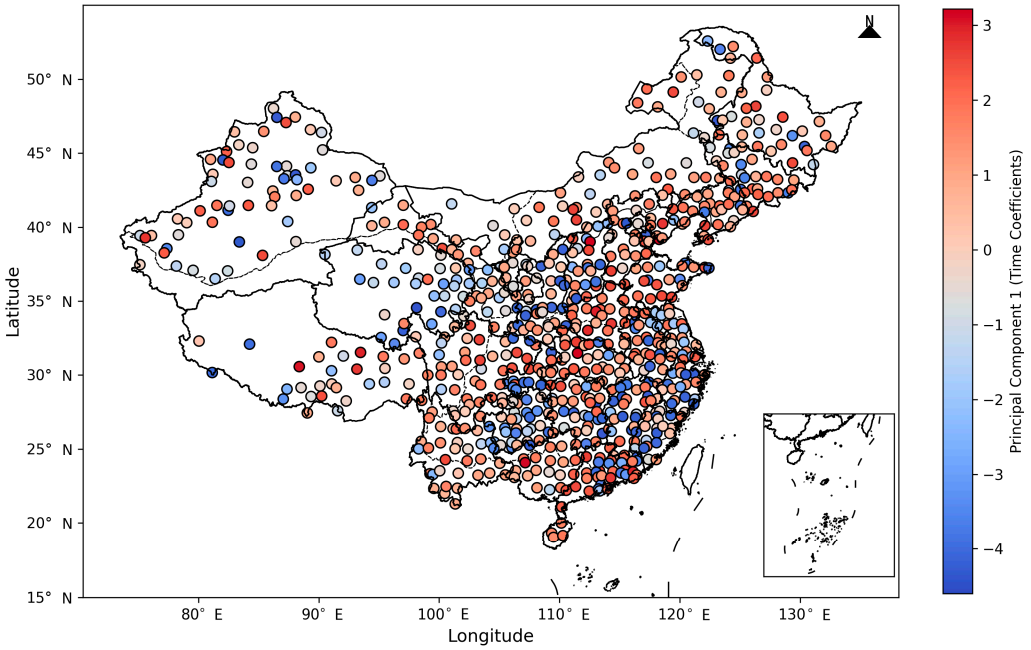

Figure 8. Time coefficient (PC1) associated with EOF1 of monthly PE anomalies. Positive PC1 corresponds to above-average PE in regions with positive EOF1 loadings and below-average PE in regions with negative loadings (and vice versa), describing the temporal evolution of the leading spatial mode.

The distribution also shows clear spatial clustering: southeastern coastal and southwestern regions generally display higher PC1 values, while many stations in northern China and the Tibetan Plateau exhibit negative values. These coherent regional patterns suggest that the first EOF mode captures a large-scale gradient in PE anomalies that varies systematically across China. The inset map provides an enlarged view of the South China Sea region, showing similar spatial consistency among island and coastal stations.

The mapped PC1 coefficients illustrate the dominant spatial polarity of the leading EOF mode and its heterogeneous expression across China, complementing the spatial loading pattern shown in EOF1.

3.5.4. Spatial Distribution of Local Moran's I for PE Values

Figure 9 presents the Local Moran's I values for annual PE, illustrating the spatial dependence of evaporation across China. Positive Local Moran's I values (warm colors) indicate locations embedded within clusters of similar PE conditions, while negative values (cool colors) mark spatial outliers where local PE values differ from surrounding stations. Most stations exhibit weak to moderately positive local spatial autocorrelation, forming broad clusters across eastern and southeastern China. These areas show coherent spatial groupings of similar PE magnitudes, suggesting locally consistent evaporation patterns. In contrast, negative Local Moran's I values are scattered primarily across northern and high-altitude regions, indicating isolated stations whose PE values differ from adjacent locations.

The distribution of Local Moran's I highlights pronounced spatial heterogeneity in PE, with contiguous clusters in some regions and fragmented patterns in others. These results complement the large-scale structures revealed by the EOF analysis and provide a finer-resolution view of local spatial organization within the national PE field. The contiguous high-autocorrelation patches in eastern and southeastern China likely reflect spatially coherent hydroclimatic forcing under the East Asian monsoon regime, whereas the fragmented and outlier-rich patterns in northern and high-elevation regions may

indicate stronger topographic gradients and localized controls (e.g., station exposure and terrain-modulated winds/radiation) that weaken spatial coherence.

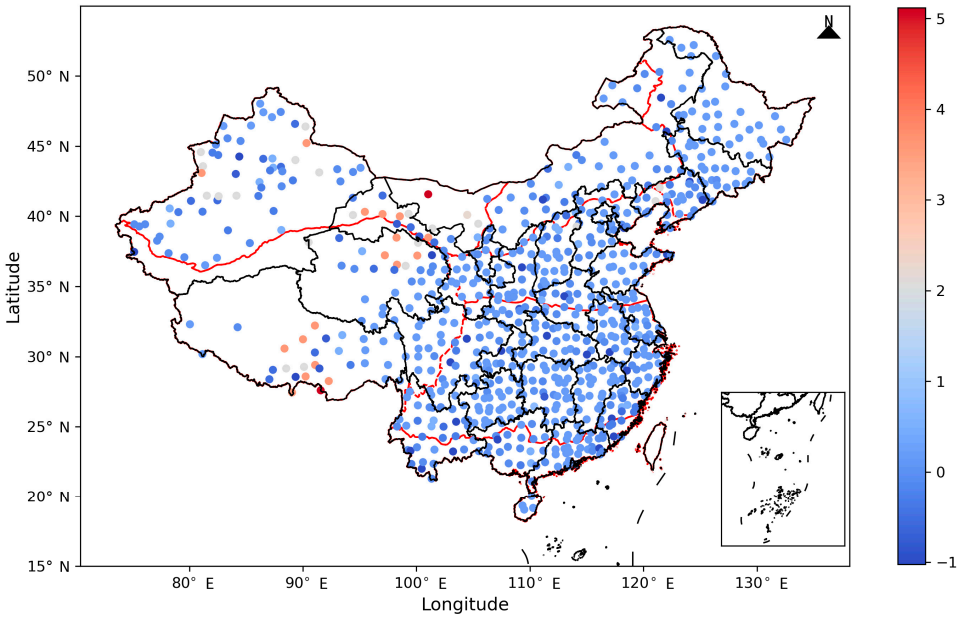

Figure 9. Spatial Distribution of Local Moran's I for PE Values.

To provide a quantitative check of the EOF interpretation, we constructed two station-derived process proxies from daily observations: an East China JJA monsoon precipitation proxy (EASM_proxy) and a Tibetan Plateau MAM–JJA mean air temperature proxy (TP_heat_proxy). Pearson correlations (two-tailed) between the leading PCs and these proxies are summarized in Table S5, and the corresponding scatter plots and standardized time series are shown in Figure S3. PC1 shows a negative association with TP_heat_proxy ($r = -0.964$, $p = 4.85 \times 10^{-10}$, $N = 17$), while correlations involving EASM_proxy are weaker (e.g., PC1 vs. EASM_proxy: $r = 0.376$, $p = 0.137$, $N = 17$). Because Pearson correlations can be affected by high-leverage years, we further conducted robustness checks using Spearman correlation and by excluding the extreme year 2018; the association weakens after excluding 2018 ($r = -0.326$, $p = 0.217$, $N = 16$), whereas the rank-based correlation remains negative for the full period ($\rho = -0.527$, $p = 0.0297$, $N = 17$). Thus, the proxy-based analysis is treated as supportive evidence for the proposed mechanisms rather than a standalone proof (Table S5; Figure S3).

3.6. Zonal Characteristics of PE

Figure 10 summarizes the zonal distribution of PE across the seven climate regions. Both monthly and annual statistics show clear differences among zones. The Mid-Temperate Arid Zone (MTA) exhibits the highest PE values, followed by the Mid-Temperate Semi-Humid Zone (MTSH). In contrast, the Northern Subtropical Humid Zone (NSTH) and Marginal Tropical Humid Zone (MTHZ) show the lowest PE levels.

The boxplots reveal substantial within-zone variability, particularly in MTA and MTSH, where wider interquartile ranges and more outliers indicate large spatial dispersion of PE among stations. Zones such as NSTH and MTHZ display narrower distributions, reflecting more spatially consistent PE conditions. The bar charts of mean PE (monthly and annual) confirm the same ordering among climate zones, demonstrating that the zonal differences are stable across temporal scales. The zonal comparison highlights pronounced spatial heterogeneity in PE among China's climate regions, with consistent ranking patterns observed at both monthly and annual resolutions.

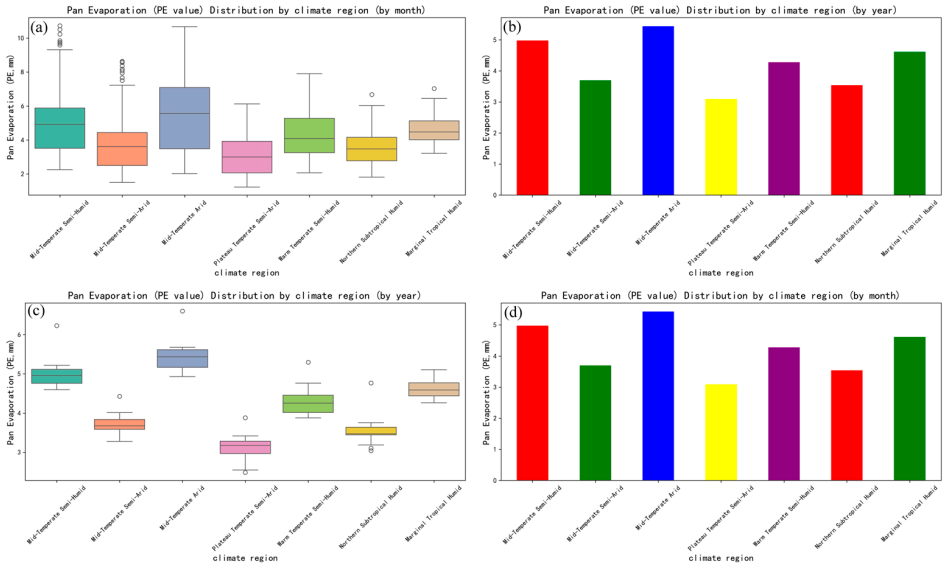

Figure 10. Zonal analysis of PE across seven climate regions in China. (**a**) Monthly PE distributions by climate zone (boxplot); (**b**) Yearly average PE values by climate zone (bar chart); (**c**) Yearly PE distributions by climate zone (boxplot); (**d**) Monthly average PE values by climate zone (bar chart).

3.7. Performance Evaluation of Random Forest Model for Predicting PE

The performance of the RF model was evaluated using an independent test set generated by a station-level split stratified by climate zone to avoid information leakage across months from the same station. Specifically, 70% of stations within each climate zone were assigned to the training set and the remaining 30% to the test set (random_state = 42), resulting in 528 training stations and 231 test stations (153,334 station-month samples in total). Figure 11 compares observed and RF-predicted monthly PE for the independent test set; predictions are generally distributed around the 1:1 line, indicating reasonable agreement. Under this strict generalization setting, the RF model achieved R^2 = 0.493 and MSE = 3.159 (RMSE = 1.777) on the independent test set. We additionally trained RF models for each climate zone to derive zonal rankings in the Supplementary Materials (Table S2).

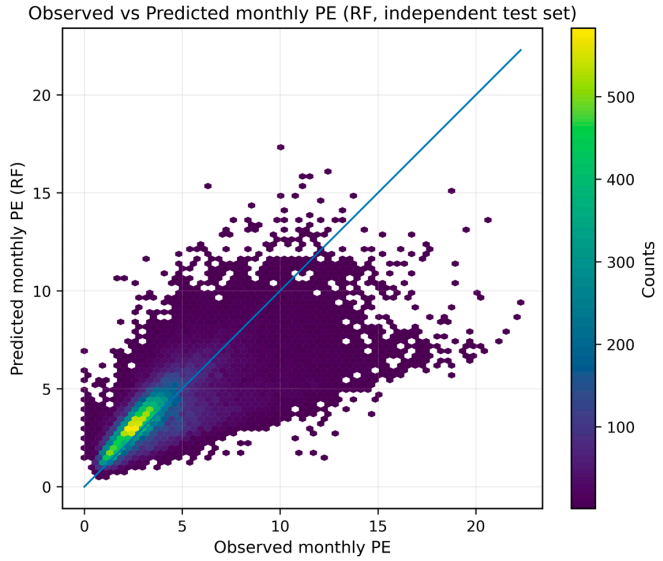

Figure 11. Comparison between observed and RF-predicted monthly pan evaporation (PE) for the independent test set generated by a station-level split stratified by climate zone. The 1:1 line is shown for reference.

To benchmark the added value of nonlinear modeling, we compared RF against linear baselines using the same station-level split (Table 1). Multiple linear regression achieved R^2 = 0.429 (MSE = 3.559, RMSE = 1.886), and ridge regression yielded comparable performance (best α = 100; R^2 = 0.429, MSE = 3.559, RMSE = 1.887). The RF model therefore improves test performance by ΔR^2 = 0.064 and reduces MSE by approximately 11%, indicating that nonlinear relationships among meteorological drivers contribute meaningfully to monthly PE variability.

Table 1. Test performance of RF and linear baseline models for monthly pan evaporation (PE) under a station-level split stratified by climate zone.

Model	R^2	MSE	RMSE
Random Forest	0.493	3.159	1.777
Linear Regression	0.429	3.559	1.886
Ridge Regression (alpha = 100.0)	0.429	3.559	1.887

3.8. Sensitivity to Within-Month Extremes Derived from Daily Observations

To further assess the robustness of the monthly modeling framework, we distinguish between the national-scale evaluation using all available monthly samples and a sensitivity experiment based on a stricter completeness subset. The performance reported above (R^2 = 0.493; MSE = 3.159) is obtained from the full monthly dataset using a station-level split stratified by climate zone. In contrast, the extremes-sensitivity experiment below is conducted on a reduced national subset of station-months for which within-month extremes metrics can be reliably derived from daily observations (requiring at least 25 valid daily records per month). This additional completeness constraint reduces sample size and can slightly affect absolute skill. Nevertheless, the resulting test performance remains comparable in magnitude, supporting that our conclusions are not driven by optimistic evaluation or by a particular subset of the data.

To evaluate whether monthly aggregation masks extreme-driven controls on PE, we conducted a sensitivity experiment using a national subset of station-months with at least 25 valid daily records (Table 2). Two within-month extremes metrics derived from daily observations were added to the baseline monthly predictors: the 95th percentile of daily wind speed (WS95) and the 95th percentile of daily air temperature (T95). Model skill improved slightly relative to the baseline model on the independent test set (Baseline: R^2 = 0.494, MSE = 3.158; Extended: R^2 = 0.503, MSE = 3.097).

Table 2. Sensitivity of RF test performance to daily derived within-month extremes metrics (WS95 and T95) on the completeness subset ($\geq$25 valid days per month).

Model	R^2	MSE	RMSE
Baseline (monthly predictors) [subset n_days $\geq$ 25]	0.494	3.158	1.775
Extended (+WS95 +T95) [subset n_days $\geq$ 25]	0.503	3.097	1.759

Permutation importance indicates that the dominant predictors remain broadly consistent between models (Figure 12). In the baseline model, RH and Tair are the top two contributors, followed by SSD. In the extended model, RH and SSD remain dominant, while the temperature effect is partly captured by T95, with a reduced importance of mean temperature (Tair). WS95 provides additional but smaller contribution. These results suggest that daily scale extremes provide incremental explanatory power but do not alter the primary driver structure at monthly climate scales, supporting the suitability of the monthly framework for the study objectives while transparently acknowledging its limitations.

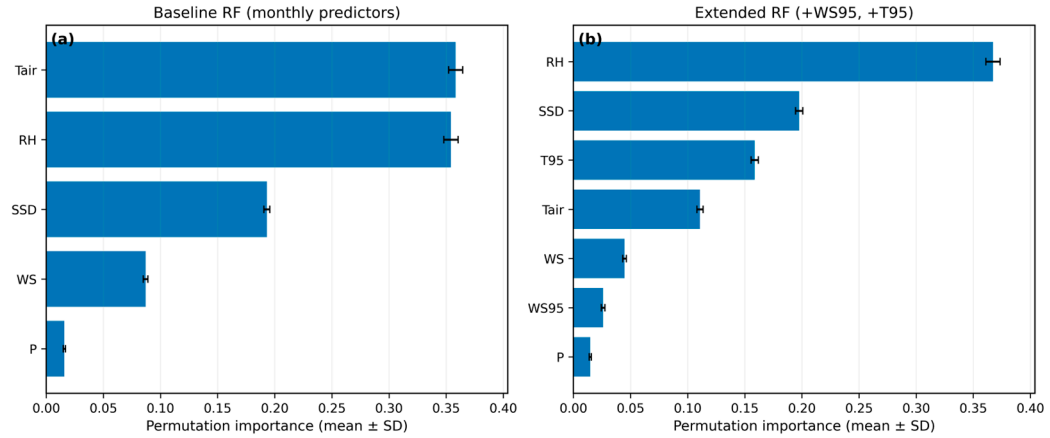

Figure 12. Permutation importance (mean ± SD) of predictors for (**a**) the baseline RF model using monthly predictors and (**b**) the extended RF model including within-month extremes metrics (WS95 and T95), computed on the independent test set of the sensitivity subset (≥25 valid daily records per month).

Urbanization information is not directly available in the station observation dataset. To evaluate the potential confounding influence of urbanization, we conducted a sensitivity analysis using nighttime lights (NTL) as an urbanization proxy. Annual NTL raster data (https://doi.org/10.11888/HumanNat.tpdc.302930, accessed on 15 December 2025) were used to extract an NTL index for each station as the buffer-mean value within a 10 km radius around the station location. The NTL index was log-transformed to reduce skewness and then merged with the monthly station dataset by station and year. The resulting subset included 744 stations (149,806 station-months) with valid NTL coverage. We compared a baseline RF model using meteorological predictors only (P, Tair, WS, RH, and SSD) with an extended RF model including the NTL proxy. Both models were evaluated using a station-wise independent split (30% of stations held out; random seed = 42), and variable importance was quantified using permutation importance on the independent test set (n_repeats = 30), reporting mean ± SD.

3.9. Climate-Zone RF Attribution and Model Performance

Climate-zone-specific RF models were evaluated using the same station-wise independent test split within each zone (Table 3). Model skill varies across zones ($R^2 \approx 0.18$–0.58), with the highest performance in MTSH ($R^2 = 0.577$) and moderate performance in MTSA/WTSH/NSTH/MTA ($R^2 \approx 0.35$–0.45). Lower skill in PTSA ($R^2 = 0.183$) and MTHZ ($R^2 = 0.186$) reflects not only smaller effective station coverage but also stronger process heterogeneity that is difficult to represent using monthly predictors alone. In PTSA, complex topography and sharp elevation gradients promote strong local circulations (e.g., valley–mountain winds) and microclimatic contrasts, while cryospheric/frozen-ground processes (snow cover, seasonal freezing–thawing and associated albedo–energy-balance effects) can modulate evaporative demand in ways not fully captured by the available monthly variables. In MTHZ, tropical convection and monsoon-driven rainfall intermittency, together with pronounced cloud/aerosol variability affecting radiative forcing and coastal land–sea interactions (including cyclone-related disturbances), can generate large sub-monthly variability and nonlinear responses, reducing monthly scale predictability. Importantly, arid MTA does not exhibit systematically worse performance than more humid zones, supporting the credibility of zonal attribution in dry regions. Because predictive skill is lower in PTSA and MTHZ, the corresponding driver-importance rankings should be interpreted as indicative rather than definitive, and we emphasize the reported importance variability (mean ± SD) as an uncertainty cue.

Table 3. Climate-zone-specific performance of the RF model for monthly PE under a station-wise independent test split (70%/30% stations within each zone).

Climate_Zone	Stations	Station_Months	R^2	MSE	RMSE
MTSH	79	16,020	0.577	2.267	1.506
MTSA	53	10,740	0.446	3.724	1.930
MTA	77	15,180	0.355	5.426	2.329
PTSA	84	16,872	0.183	2.899	1.703
NSTH	129	26,160	0.367	3.139	1.772
WTSH	270	54,790	0.423	2.250	1.500
MTHZ	67	13,572	0.186	2.762	1.662

Driver importance shows clear contrasts along the humidity gradient (Figure 13). Across all zones, air temperature (Tair) is consistently the dominant predictor (normalized importance ≈ 0.37–0.60). Relative humidity (RH) becomes comparatively more influential in humid/sub-humid zones (e.g., NSTH and MTSH), indicating stronger humidity constraints on evaporative demand. Sunshine duration (SSD), representing radiative forcing, contributes more strongly in MTA and MTHZ (both ≈ 0.36), highlighting region-dependent radiation controls. Wind speed (WS) plays a secondary but non-negligible role, particularly in PTSA and MTHZ. In contrast, precipitation (P) shows minimal direct importance in the monthly framework, suggesting that its influence is largely mediated through humidity and radiation-related conditions.

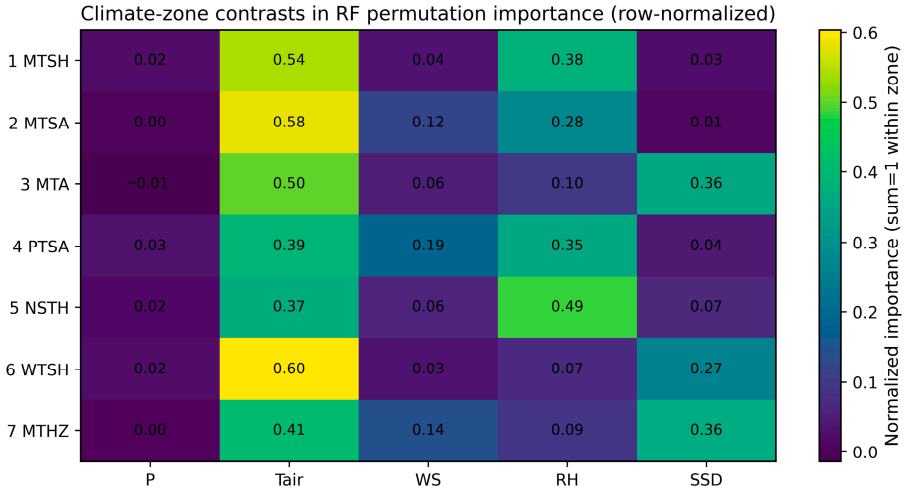

Figure 13. Climate-zone contrasts in RF permutation importance (row-normalized within each zone) for monthly PE predictors (P, Tair, WS, RH, and SSD).

3.10. Urbanization Sensitivity Using Nighttime Lights

To assess whether excluding urbanization could bias the RF attribution, we conducted a sensitivity experiment by adding an NTL-based urbanization proxy to the monthly meteorological predictor set for the subset of stations with NTL coverage (744 stations; 149,806 station-months). Incorporating NTL slightly improves independent-test performance relative to the meteorology-only model (Baseline: R^2 = 0.4502, MSE = 3.0524, RMSE = 1.7471; Extended: R^2 = 0.4545, MSE = 3.0289, RMSE = 1.7404; Table S3). Permutation importance indicates that the dominant drivers remain temperature, relative humidity, and sunshine duration, while the NTL proxy contributes only a small additional component (Figure S1). Overall, the results suggest that urbanization provides incremental explanatory power but does not alter the primary driver structure identified at monthly climate scales.

3.11. Meteorological Context of the 2018 PE Increase

A pronounced increase in PE is observed in 2018 in the national annual series (Figure 2b). To interpret this event, we quantified 2018 anomalies relative to the 2002–2017 baseline using station observations (Table S4; Figure S2). Nationally, PE shows a positive anomaly of +0.877, coinciding with markedly warmer conditions (Tair: +3.388) and substantially reduced precipitation (P: −59.404), indicating a warmer and drier background that favors enhanced evaporative demand. Wind speed exhibits a modest positive anomaly (WS: +0.120), whereas relative humidity changes are negligible at the national scale (RH: +0.004). Sunshine duration anomalies display strong spatial heterogeneity across climate zones (Figure S2), suggesting region-dependent radiative forcing during 2018. Overall, the 2018 PE surge is most coherently explained by the combined effects of anomalous warming and widespread precipitation deficits, with additional regional modulation by wind and radiation anomalies, consistent with the RF-identified dominant drivers. These local anomalies motivate a broader discussion of the large-scale climate modes that may have preconditioned the 2018 warm–dry background (Section 4.4).

4. Discussion

4.1. Spatiotemporal Trends of PE

Our trend analyses reveal a pronounced decline in PE across northern China, with the strongest decreases concentrated in the Mid-Temperate Arid (MTA) and Plateau Temperate Semi-Arid (PTSA) regions. This northward-drying/declining pattern is consistent with previous reports of long-term PE decreases in inland northern China (e.g., Li et al. [19]; Fu et al. [10]). In our RF attribution, the decline is most coherently interpreted through changes in key aerodynamic–thermodynamic controls, particularly wind speed and temperature–humidity conditions, together with radiation variability represented by sunshine duration. Notably, the RF attribution identifies wind speed as a dominant driver in the arid and semi-arid zones that largely occupy northern China (MTA/MTSA/PTSA; Tables 3 and S2). This aligns with the reported decline ('stilling') of near-surface winds across northern China in recent decades, which weakens aerodynamic forcing and can therefore contribute directly to the observed PE decrease. Such wind changes may reflect a combination of large-scale circulation variability (e.g., changes in the mid-latitude westerlies/East Asian jet and monsoon–westerly contrasts) and regional surface influences, consistent with the circulation-regime interpretation implied by our EOF patterns and local Moran's I diagnostics. The southern and coastal regions show stronger interannual variability, consistent with earlier studies emphasizing the roles of radiation and wind in modulating PE variability in humid basins such as the Yangtze River Basin [4].

Beyond the meteorological controls quantified here, land-surface changes and human activities may modulate PE indirectly by altering near-surface wind fields, surface roughness, and radiative conditions. For example, land-use changes (afforestation, irrigation expansion, and water management) have been linked to changes in evaporative demand and its drivers [11]. However, our sensitivity tests (within-month extremes; NTL proxy) indicate that the dominant driver structure inferred from monthly meteorological predictors remains robust, while acknowledging that some long-term signals embedded in wind and temperature may partially reflect land-surface and urbanization influences. In addition, the spatial modes identified by EOF and local Moran's I imply that PE variability is organized by circulation-regime contrasts between monsoon-influenced eastern China and westerly/plateau-influenced western China. Such circulation shifts can systematically modulate the RF-dominant controls—especially RH and SSD via cloudiness/moisture transport and WS via pressure-gradient forcing and terrain–flow interactions—thereby producing coherent regional structures rather than isolated station signals.

4.2. Climate Zone Specific Variability

The zonal analysis highlights the importance of regional climate regimes in shaping PE patterns. Higher PE values in the Mid-Temperate Arid (MTA) and Mid-Temperate Semi-Humid (MTSH) zones are consistent with the findings of Liu et al. [53], who reported strong control of radiation and wind speed on evaporation in these regions. In contrast, the Northern Subtropical Humid (NSTH) and Marginal Tropical Humid (MTHZ) zones exhibit lower PE due to persistent high humidity and frequent cloud cover, which reduces sunshine duration (SSD) and suppresses evaporative demand. This is quantitatively supported by the zonal RF importance ranking, where wind speed consistently appears among the top predictors in MTA/MTSA/PTSA (Tables 3 and S2).

The zonal RF models further demonstrate that the relative importance of drivers varies systematically along the humidity gradient. In arid and semi-arid regions (e.g., MTA/MTSA/PTSA), PE variability is more strongly conditioned by aerodynamic forcing and threshold-like responses involving wind speed and radiation–humidity interactions, whereas in humid zones (e.g., NSTH/MTHZ) PE is more consistently constrained by humidity and reduced available radiation (lower SSD under frequent cloud cover). These findings support the notion that nonlinear interactions among meteorological drivers are especially important in water-limited climates [9] and help explain the observed contrasts in PE levels and variability among climate zones.

4.3. Climatic Interpretation of EOF Modes and Local Spatial Autocorrelation

The spatial diagnostics (EOF and Local Moran's I) indicate that PE variability across China is organized into coherent regional structures, rather than arising solely from site-specific noise. The leading EOF modes explain a large fraction of the variance (EOF1: 46.0%; EOF2: 20.1%), suggesting that a small number of large-scale processes governs the dominant spatiotemporal variability.

A key feature is the northeast–west/Tibetan Plateau dipole described in the EOF patterns, which points to contrasts between the monsoon-influenced eastern/northeastern regions and the westerly- and topography-controlled western interior and Plateau. Mechanistically, variability in East Asian monsoon moisture transport and cloudiness can alter regional humidity (RH) and radiative availability (SSD) over northeastern/eastern China, whereas changes in the mid-latitude westerlies and the East Asian jet—together with Tibetan Plateau thermal–dynamic effects—can modulate near-surface wind speed (WS) and radiation conditions over western China and the Plateau. These circulation-linked pathways directly target the same dominant controls identified by the RF attribution (Tair/RH/SSD and WS), providing a physical basis for the observed opposite-phase spatial structure. The proxy-based quantitative check (Table S5; Figure S3) provides supportive evidence for this interpretation. Notably, PC1 shows a negative association with the Plateau thermal proxy, although the Pearson correlation is influenced by the extreme year 2018. Therefore, we use this result as supplementary support and keep the mechanistic discussion primarily grounded in the spatial patterns and physical consistency rather than a single correlation metric.

The Local Moran's I results further support the climatic significance of these patterns by showing spatial clustering of PE signals, implying that neighboring stations often share similar PE behavior within contiguous climatic–topographic settings. More spatial coherence is expected where stations are jointly influenced by a common circulation regime and have relatively homogeneous surface–atmosphere coupling, whereas fragmented patterns and outliers can occur in regions with strong terrain gradients and locally modulated winds/radiation. Together, the EOF modes and local spatial autocorrelation suggest that

PE variability is shaped by the interaction between large-scale circulation regimes and regional land–atmosphere processes, rather than being purely random in space.

4.4. Meteorological Context of the 2018 PE Increase

A pronounced increase in PE is observed in 2018 in the national annual series (Figure 2b). To interpret this event, we quantified 2018 anomalies relative to the 2002–2017 baseline using station observations (Table S4; Figure S2). Nationally, PE shows a positive anomaly of +0.877, coinciding with markedly warmer conditions (Tair: +3.388) and substantially reduced precipitation (P: −59.404), indicating a warmer and drier background that favors enhanced evaporative demand. Wind speed exhibits a modest positive anomaly (WS: +0.120), whereas relative humidity changes are negligible at the national scale (RH: +0.004). Sunshine duration anomalies display strong spatial heterogeneity across climate zones (Figure S2), suggesting region-dependent radiative forcing during 2018. Overall, the 2018 PE surge is most coherently explained by the combined effects of anomalous warming and widespread precipitation deficits, with additional regional modulation by wind and radiation anomalies, consistent with the RF-identified dominant drivers.

From a large-scale perspective, the 2018 anomaly occurred against a backdrop of prominent ocean–atmosphere variability. The year followed a weak La Niña in boreal winter 2017/18 and transitioned toward ENSO-neutral conditions, with indications of El Niño development later in 2018. In addition, the Indian Ocean Dipole (IOD) became above-average during late 2018. These modes can modulate East Asian circulation and moisture transport—via changes in monsoon–westerly contrasts, jet positioning, and regional pressure-gradient forcing—thereby providing a physically plausible pathway to the widespread precipitation deficits and anomalous warming reflected in our station-based anomalies (Table S4; Figure S2). We emphasize that this provides climatic context rather than a formal attribution; quantifying the linkage between PE variability (and the leading EOF modes) and standard climate indices is a valuable direction for future work.

4.5. Random Forest Model Performance

The RF model shows moderate predictive skill for monthly PE under a strict station-level independent test stratified by climate zone (R^2 = 0.493; MSE = 3.159; RMSE = 1.777). This level of skill is consistent with previous evidence that machine-learning approaches can outperform traditional regression methods for evaporation-related prediction tasks (e.g., Yaseen et al. [54]). Importantly, RF also outperforms linear baselines evaluated under the same splitting protocol (multiple linear regression: R^2 = 0.429, RMSE = 1.886; ridge regression: R^2 = 0.429, RMSE = 1.887), indicating that nonlinear relationships among meteorological drivers contribute meaningfully to monthly PE variability. While the model captures a substantial fraction of the observed variability, discrepancies at high PE values suggest challenges in representing extremes or threshold behavior using monthly predictors alone—a limitation also noted by Wang et al. [55]. These deviations may reflect nonlinear or threshold-driven processes that require additional environmental inputs (e.g., radiation components beyond sunshine duration, aerosol/cloud effects, land-surface conditions, or urbanization proxies) or more advanced learning architectures to further improve robustness under extreme conditions. This limitation is further examined through our sensitivity experiment incorporating within-month extremes (WS95 and T95), which yields modest skill gains while preserving the dominant driver structure (Section 3.8).

Urbanization may influence PE indirectly by modifying local near-surface meteorological conditions, including reduced wind speed due to increased roughness and altered station exposure, and increased air temperature due to the urban heat island effect. Because our primary RF attribution is based on observed meteorological predictors, part of the

long-term variability in wind speed and temperature may embed urbanization-related signals. The NTL sensitivity analysis provides an explicit quantitative check on this potential confounding influence and indicates that, while urbanization contributes modest incremental information, the dominant attribution results (temperature, humidity, and sunshine duration as leading drivers) remain robust within the evaluated subset.

4.6. Limitations and Future Directions

Although this study integrates trend detection, multi-scale decomposition, spatial statistics, and machine-learning attribution, several limitations should be noted. First, pan evaporation (PE) reflects atmospheric evaporative demand measured by a standardized pan and does not fully represent actual evapotranspiration or land-surface water constraints. Future work should integrate additional land-surface and ecohydrological variables (e.g., soil moisture, vegetation indices, land surface temperature, and actual evapotranspiration products) to better link PE variability with surface energy–water balance processes and to improve physical interpretability across heterogeneous landscapes.

Second, disentangling urbanization effects remains challenging because a consistent urban–rural classification and station-matched urbanization indicators are not available for all sites. Nevertheless, we conducted an NTL-based sensitivity analysis for the subset of stations with valid nighttime-lights coverage, which indicates that urbanization proxies provide modest incremental explanatory information while the dominant meteorological driver structure remains robust. This is consistent with evidence that urban stations may exhibit altered evaporative conditions due to urban heat island effects and modified surface energy balance (e.g., Fan et al. [15]). Future work will refine anthropogenic attribution by combining multiple urbanization datasets (e.g., impervious surface fraction, population density, and urban–rural classification) and by explicitly testing their interactions with wind, humidity, and radiation-related controls.

Third, our primary analyses use monthly aggregation to emphasize interannual–decadal variability and to ensure temporal completeness across the national station network. Monthly aggregation, however, can damp short-duration extremes and may underrepresent nonlinear daily responses of PE to heatwaves or strong wind events. To partially address this, we performed a sensitivity experiment using within-month extremes metrics derived from daily observations (WS95 and T95) for a completeness subset, showing modest skill gains without altering the dominant driver structure. Future work will extend daily resolution analyses to better characterize sub-seasonal variability, compound extremes, and event-based drivers of anomalous years.

Finally, our spatial diagnostics are based on station observations rather than a continuous gridded field; uneven station density may influence the apparent spatial detail of EOF modes and local spatial autocorrelation patterns. Future work could combine station records with spatially continuous gridded products (e.g., reanalysis or satellite-based datasets) to improve spatial representativeness and to support more explicit circulation- and land-surface-based interpretations of the observed spatial structures. Extending the analysis beyond 2018 and integrating future climate projections would also allow a more comprehensive assessment of evaporation dynamics under changing climate conditions.

5. Conclusions

This study provides a comprehensive assessment of the spatiotemporal variability of pan evaporation (PE) across China from 2002 to 2018 by integrating trend analysis, multi-scale decomposition, spatial statistics, and machine learning methods. The results reveal pronounced regional heterogeneity: northern temperate arid and semi-arid regions experienced a persistent decline in PE, while southern and coastal regions exhibited stronger

interannual variability and stable seasonal cycles. These contrasting patterns highlight the differing regional responses of evaporative demand to ongoing climatic shifts.

Zonal comparisons further demonstrate that PE varies systematically across China's seven climate regions. Higher PE levels occur in mid-temperate arid and semi-humid zones, whereas subtropical and tropical humid zones exhibit lower values. These consistent spatial differences underscore the critical role of regional climate regimes in modulating evaporation patterns.

The Random Forest model captured a substantial fraction of monthly PE variability under a strict station-level independent test stratified by climate zone (R^2 = 0.493, RMSE = 1.777), and consistently outperformed linear baselines ($R^2 \approx 0.429$), supporting its suitability for nonlinear attribution and prediction of PE across diverse climatic environments.

Several limitations should be noted. PE alone cannot fully represent actual evapotranspiration, and additional variables—such as soil moisture, vegetation indices, and land-surface characteristics—should be incorporated in future research. Urbanization effects were not explicitly considered and warrant further investigation, especially given their growing influence on local evaporation dynamics.

This study enhances understanding of how PE responds to climatic and regional controls in China and provides a framework for improving evaporation prediction. The findings can support water resource management, agricultural planning, and climate adaptation strategies tailored to region-specific environmental and hydrological conditions.

Supplementary Materials: The following supporting information can be downloaded at: https://www.mdpi.com/article/10.3390/atmos17010073/s1, Figure S1: Permutation importance (mean ± SD) for (a) the baseline RF model using meteorological predictors only and (b) the extended RF model including the NTL-based urbanization proxy, computed on the independent test set of the NTL subset; Figure S2: Zonal anomalies in 2018 relative to 2002–2017; Figure S3: Relationships between PC1 of annual PE anomalies and station-derived process proxies. (a) Scatter plot of stand-ardized PC1 versus TP_heat_proxy (Tibetan Plateau MAM–JJA mean air temperature averaged across Plateau stations). (b) Standardized time series of PC1 and TP_heat_proxy (2002–2018). (c) Scatter plot of standardized PC1 versus EASM_proxy (East China JJA precipitation averaged across monsoon-region stations). (d) Standardized time series of PC1 and EASM_proxy. Pearson r (two-tailed) is annotated in each panel. Robustness checks indicate sensi-tivity to the high-leverage year 2018 for PC1–TP_heat_proxy (Spearman ρ = −0.527, p = 0.0297, N = 17; exclud-ing 2018: r = −0.326, p = 0.217, N = 16; ρ = −0.432, p = 0.094, N = 16); Table S1: Random Forest hyperparameters used in this study; Table S2: Variable-importance ranking of meteorological drivers of monthly pan evaporation (PE) across seven climate zones; Table S3: Sensitivity of RF test performance to an urbanization proxy (nighttime lights, NTL) for the subset of stations with valid NTL coverage (744 stations; 149,806 station-months), evaluated using a station-wise independent test split; Table S4: National and climate-zone anomalies in 2018 for pan evaporation (PE) and key meteorological drivers relative to the 2002–2017 baseline; Table S5: Pearson correlations between the leading EOF principal components (PC1–PC2) of annual PE anomalies and sta-tion-derived process proxies representing (i) East China monsoon-season precipitation (EASM_proxy; JJA) and (ii) Tibetan Plateau thermal conditions (TP_heat_proxy; MAM–JJA). Correlations are reported for contemporaneous (Lag_years = 0) and one-year lead (Lag_years = 1) relationships.

Author Contributions: Conceptualization, S.L.; methodology, S.L.; validation, X.L.; formal analysis, S.L.; investigation, S.L.; resources, X.L.; data curation, X.L.; writing—original draft preparation, S.L.; writing—review and editing, X.L.; visualization, S.L.; supervision, X.L.; project administration, X.L.; funding acquisition, X.L. All authors have read and agreed to the published version of the manuscript.

Funding: This research was funded by the National Natural Science Foundation of China (42301414) and the China Postdoctoral Science Foundation (2023M732959).

Institutional Review Board Statement: Not applicable.

Informed Consent Statement: Not applicable.

Data Availability Statement: The data are available from the corresponding author on reasonable request.

Acknowledgments: The authors would like to thank all the scientists, engineers, and students. We appreciate all reviewers and editors for their comments on this paper.

Conflicts of Interest: The authors declare no conflicts of interest.

References

1. Roderick, M.L.; Rotstayn, L.D.; Farquhar, G.D.; Hobbins, M.T. On the Attribution of Changing Pan Evaporation. *Geophys. Res. Lett.* **2007**, *34*, L17403. [CrossRef]
2. Roderick, M.L.; Farquhar, G.D. The Cause of Decreased Pan Evaporation over the Past 50 Years. *Science* **2002**, *298*, 1410–1411. [CrossRef]
3. Zuo, H.; Li, D.; Hu, Y.; Bao, Y.; Lü, S. Characteristics of Climatic Trends and Correlation between Pan-Evaporation and Environmental Factors in the Last 40 Years over China. *Chin. Sci. Bull.* **2005**, *50*, 1235–1241. [CrossRef]
4. Xu, C.-Y.; Gong, L.; Jiang, T.; Chen, D.; Singh, V.P. Analysis of Spatial Distribution and Temporal Trend of Reference Evapotranspiration and Pan Evaporation in Changjiang (Yangtze River) Catchment. *J. Hydrol.* **2006**, *327*, 81–93. [CrossRef]
5. Mao, S.; Lu, H.; Zhang, L.; Liu, P.; Cheng, L. Reversed Trends in Pan and Actual Evaporation in China during 1960–2019. *J. Hydrol.* **2025**, *653*, 132810. [CrossRef]
6. Donohue, R.J.; Roderick, M.L.; McVicar, T.R. Can Dynamic Vegetation Information Improve the Accuracy of Budyko's Hydrological Model? *J. Hydrol.* **2010**, *390*, 23–34. [CrossRef]
7. Hu, J.; Zhao, G.; Li, P.; Mu, X. Variations of Pan Evaporation and Its Attribution from 1961 to 2015 on the Loess Plateau, China. *Nat. Hazards* **2022**, *111*, 1199–1217. [CrossRef]
8. Niu, Z.; Wang, L.; Chen, X.; Yang, L.; Feng, L. Spatiotemporal Distributions of Pan Evaporation and the Influencing Factors in China from 1961 to 2017. *Environ. Sci. Pollut. Res.* **2021**, *28*, 68379–68397. [CrossRef]
9. Wang, H.; Sun, F.; Wang, T.; Feng, Y.; Liu, F.; Liu, W. On the Pattern and Attribution of Pan Evaporation over China (1951–2021). *J. Hydrometeorol.* **2023**, *24*, 2023–2033. [CrossRef]
10. Fu, G.; Charles, S.P.; Yu, J. A Critical Overview of Pan Evaporation Trends over the Last 50 Years. *Clim. Change* **2009**, *97*, 193–214. [CrossRef]
11. Yang, H.; Yang, D. Climatic Factors Influencing Changing Pan Evaporation across China from 1961 to 2001. *J. Hydrol.* **2012**, *414–415*, 184–193. [CrossRef]
12. Li, J.; Gao, B. How Urbanization Affects Pan Evaporation in China? *Urban Clim.* **2023**, *49*, 101536. [CrossRef]
13. Chen, H.; Huang, J.J.; Li, H.; Wei, Y.; Zhu, X. Revealing the Response of Urban Heat Island Effect to Water Body Evaporation from Main Urban and Suburb Areas. *J. Hydrol.* **2023**, *623*, 129687. [CrossRef]
14. Feng, Y.; Jia, Y.; Zhang, Q.; Gong, D.; Cui, N. National-Scale Assessment of Pan Evaporation Models across Different Climatic Zones of China. *J. Hydrol.* **2018**, *564*, 314–328. [CrossRef]
15. Fan, D.; Yu, H.; Liu, G.; Yang, R.; Li, X.; Wang, L. Effect of Urbanization on the Long-Term Change in Pan Evaporation: A Case Study of the Nanpan River Basin in China. *Ecol. Indic.* **2022**, *145*, 109631. [CrossRef]
16. Stephens, C.M.; McVicar, T.R.; Johnson, F.M.; Marshall, L.A. Revisiting Pan Evaporation Trends in Australia a Decade On. *Geophys. Res. Lett.* **2018**, *45*, 11164–11172. [CrossRef]
17. Chen, H.; Huang, J.J.; Dash, S.S.; McBean, E.; Wei, Y.; Li, H. Assessing the Impact of Urbanization on Urban Evapotranspiration and Its Components Using a Novel Four-Source Energy Balance Model. *Agric. For. Meteorol.* **2022**, *316*, 108853. [CrossRef]
18. Jin, K.; Qin, M.; Tang, R.; Huang, X.; Hao, L.; Sun, G. Urban–Rural Interface Dominates the Effects of Urbanization on Watershed Energy and Water Balances in Southern China. *Landsc. Ecol.* **2023**, *38*, 3869–3887. [CrossRef]
19. Li, J.; Li, Y.; Wang, X.; Ma, Z. Exploring the Spatial-Temporal Patterns, Drivers, and Response Strategies of Desertification in the Mu Us Desert from Multiple Regional Perspectives. *Sustain* **2024**, *16*, 9154. [CrossRef]
20. Fu, J.; Gong, Y.; Zheng, W.; Zou, J.; Zhang, M.; Zhang, Z.; Qin, J.; Liu, J.; Quan, B. Spatial-Temporal Variations of Terrestrial Evapotranspiration across China from 2000 to 2019. *Sci. Total Environ.* **2022**, *825*, 153951. [CrossRef]
21. Zhu, W.; Tian, S.; Wei, J.; Jia, S.; Song, Z. Multi-Scale Evaluation of Global Evapotranspiration Products Derived from Remote Sensing Images: Accuracy and Uncertainty. *J. Hydrol.* **2022**, *611*, 127982. [CrossRef]
22. Gezici, K.; Katipoğlu, O.M.; Şengül, S. Hybrid Machine Learning Models for Groundwater Level Prediction in a Snow-Dominated Region: An Evaluation of EEMD, VMD and EWT Decomposition Techniques. *Hydrol. Process.* **2024**, *38*, e15169. [CrossRef]
23. Yan, Z.; Li, Z.; Baetz, B. Evapotranspiration Estimation with the Budyko Framework for Canadian Watersheds. *Hydrology* **2024**, *11*, 191. [CrossRef]

24. Shamir, E.; Mendoza Fierro, L.; Mohsenzadeh Karimi, S.; Pelak, N.; Tarouilly, E.; Chang, H.I.; Castro, C.L. Climate Change Projections of Potential Evapotranspiration for the North American Monsoon Region. *Hydrology* **2024**, *11*, 83. [CrossRef]
25. Dai, Q.; Chen, H.; Cui, C.; Li, J.; Sun, J.; Ma, Y.; Peng, X.; Wang, Y.; Hu, X. Spatiotemporal Characteristics of Actual Evapotranspiration Changes and Their Climatic Causes in China. *Remote Sens.* **2024**, *16*, 8. [CrossRef]
26. Wang, Z.; Xie, P.; Lai, C.; Chen, X.; Wu, X.; Zeng, Z.; Li, J. Spatiotemporal Variability of Reference Evapotranspiration and Contributing Climatic Factors in China during 1961–2013. *J. Hydrol.* **2017**, *544*, 97–108. [CrossRef]
27. Xu, L.; Zheng, C.; Ma, Y. Variations in Precipitation Extremes in the Arid and Semi-Arid Regions of China. *Int. J. Climatol.* **2021**, *41*, 1542–1554. [CrossRef]
28. Shi, P.J.; Sun, S.; Wang, M.; Li, N.; Wang, J.A.; Jin, Y.Y.; Gu, X.T.; Yin, W.X. Climate Change Regionalization in China (1961–2010). *Sci. China Earth Sci.* **2014**, *57*, 2676–2689. [CrossRef]
29. Zhang, Q.; Qi, T.; Li, J.; Singh, V.P.; Wang, Z. Spatiotemporal Variations of Pan Evaporation in China during 1960-2005: Changing Patterns and Causes. *Int. J. Climatol.* **2015**, *35*, 903–912. [CrossRef]
30. Liu, X.; Wang, S.; Zhou, Y.; Wang, F.; Li, W.; Liu, W. Regionalization and Spatiotemporal Variation of Drought in China Based on Standardized Precipitation Evapotranspiration Index (1961–2013). *Adv. Meteorol.* **2015**, *2015*, 950262. [CrossRef]
31. Fan, J.; Wu, L.; Zhang, F.; Xiang, Y.; Zheng, J. Climate Change Effects on Reference Crop Evapotranspiration across Different Climatic Zones of China during 1956–2015. *J. Hydrol.* **2016**, *542*, 923–937. [CrossRef]
32. Yang, P.; Xia, J.; Luo, X.; Meng, L.; Zhang, S.; Cai, W.; Wang, W. Impacts of Climate Change-Related Flood Events in the Yangtze River Basin Based on Multi-Source Data. *Atmos. Res.* **2021**, *263*, 105819. [CrossRef]
33. Liu, B.; Xu, M.; Henderson, M.; Gong, W. A Spatial Analysis of Pan Evaporation Trends in China, 1955-2000. *J. Geophys. Res. D Atmos.* **2004**, *109*, D15102. [CrossRef]
34. Xiong, A.Y.; Liao, J.; Xu, B. Reconstruction of a Daily Large-Pan Evaporation Dataset over China. *J. Appl. Meteorol. Climatol.* **2012**, *51*, 1265–1275. [CrossRef]
35. Hao, Z.; Jin, J.; Xia, R.; Tian, S.; Yang, W.; Liu, Q.; Zhu, M.; Ma, T.; Jing, C.; Zhang, Y. CCAM: China Catchment Attributes and Meteorology Dataset. *Earth Syst. Sci. Data* **2021**, *13*, 5591–5616. [CrossRef]
36. Li, Y.; Liu, C.; Liang, K. Spatial Patterns and Influence Factors of Conversion Coefficients between Two Typical Pan Evaporimeters in China. *Water* **2016**, *8*, 422. [CrossRef]
37. Shen, J.; Yang, H.; Li, S.; Liu, Z.; Cao, Y.; Yang, D. Revisiting the Pan Evaporation Trend in China During 1988–2017. *J. Geophys. Res. Atmos.* **2022**, *127*, e2022JD036489. [CrossRef]
38. Feng, S.; Hu, Q.; Qian, W. Quality Control of Daily Meteorological Data in China, 1951–2000: A New Dataset. *Int. J. Climatol.* **2004**, *24*, 853–870. [CrossRef]
39. Carolina, N.; Chang, Y.; Burningham, H. Gap Filling of Daily Weather Data Using Spatial Interpolation Techniques and Neural Network Methods. *J. Coast. Res.* **2024**, *113*, 463–467. [CrossRef]
40. Afrifa-Yamoah, E.; Mueller, U.A.; Taylor, S.M.; Fisher, A.J. Missing Data Imputation of High-Resolution Temporal Climate Time Series Data. *Meteorol. Appl.* **2020**, *27*, e1873. [CrossRef]
41. Hawinkel, P.; Swinnen, E.; Lhermitte, S.; Verbist, B.; Van Orshoven, J.; Muys, B. A Time Series Processing Tool to Extract Climate-Driven Interannual Vegetation Dynamics Using Ensemble Empirical Mode Decomposition (EEMD). *Remote Sens. Environ.* **2015**, *169*, 375–389. [CrossRef]
42. Yang, K.; Zhang, Q.; Shi, Y. Interannual Variability of the Evaporation Duct over the South China Sea and Its Relations with Regional Evaporation. *J. Geophys. Res. Oceans* **2017**, *122*, 6698–6713. [CrossRef]
43. Kliengchuay, W.; Mingkhwan, R.; Kiangkoo, N.; Suwanmanee, S.; Sahanavin, N.; Kongpran, J.; Aung, H.W.; Tantrakarnapa, K. Analyzing Temperature, Humidity, and Precipitation Trends in Six Regions of Thailand Using Innovative Trend Analysis. *Sci. Rep.* **2024**, *14*, 7800. [CrossRef]
44. Gao, H.; Jin, J. Analysis of Water Yield Changes from 1981 to 2018 Using an Improved Mann-Kendall Test. *Remote Sens.* **2022**, *14*, 2009. [CrossRef]
45. Liu, Y.; Wang, Q.; Yao, X.; Jiang, Q.; Yu, J.; Jiang, W. Variation in Reference Evapotranspiration over the Tibetan Plateau during 1961–2017: Spatiotemporal Variations, Future Trends and Links to Other Climatic Factors. *Water* **2020**, *12*, 3178. [CrossRef]
46. Wang, G.; Li, X.; Zhao, K.; Li, Y.; Sun, X. Quantifying the Spatio-Temporal Variations and Impacts of Factors on Vegetation Water Use Efficiency Using STL Decomposition and Geodetector Method. *Remote Sens.* **2022**, *14*, 5926. [CrossRef]
47. Torrence, C.; Compo, G.P. A Practical Guide to Wavelet Analysis. *Bull. Am. Meteorol. Soc.* **1998**, *79*, 61–78. [CrossRef]
48. Wu, Z.; Huang, N.E. Ensemble Empirical Mode Decomposition: A Noise-Assisted Data Analysis Method. *Adv. Adapt. Data Anal.* **2009**, *1*, 1–41. [CrossRef]
49. Cleveland, R.B.; Cleveland, W.S.; McRae, J.E.; Terpenning, I. STL: A Seasonal-Trend Decomposition. *J. Off. Stat.* **1990**, *6*, 3–73. [CrossRef]
50. Hannachi, A.; Jolliffe, I.T.; Stephenson, D.B. Empirical Orthogonal Functions and Related Techniques in Atmospheric Science: A Review. *Int. J. Climatol.* **2007**, *27*, 1119–1152. [CrossRef]

51. Jollife, I.T.; Cadima, J. Principal Component Analysis: A Review and Recent Developments. *Philos. Trans. R. Soc. A Math. Phys. Eng. Sci.* **2016**, *374*, 20150202. [CrossRef] [PubMed]
52. Anselin, L. Local Indicators of Spatial Association—LISA. *Geogr. Anal.* **1995**, *27*, 93–115. [CrossRef]
53. Liu, X.; Zheng, H.; Zhang, M.; Liu, C. Identification of Dominant Climate Factor for Pan Evaporation Trend in the Tibetan Plateau. *J. Geogr. Sci.* **2011**, *21*, 594–608. [CrossRef]
54. Yaseen, Z.M.; Al-Juboori, A.M.; Beyaztas, U.; Al-Ansari, N.; Chau, K.W.; Qi, C.; Ali, M.; Salih, S.Q.; Shahid, S. Prediction of Evaporation in Arid and Semi-Arid Regions: A Comparative Study Using Different Machine Learning Models. *Eng. Appl. Comput. Fluid Mech.* **2020**, *14*, 70–89. [CrossRef]
55. Wang, L.; Kisi, O.; Hu, B.; Bilal, M.; Zounemat-Kermani, M.; Li, H. Evaporation Modelling Using Different Machine Learning Techniques. *Int. J. Climatol.* **2017**, *37*, 1076–1092. [CrossRef]